Nanoscale

PAPER

View Article Online
View Journal | View Issue

Cite this: *Nanoscale*, 2016, **8**, 8696

2D-MoO_3 nanosheets for superior gas sensors†

Fangxu Ji,[a] Xianpei Ren,[a] Xiaoyao Zheng,[a] Yucheng Liu,[a] Liuqing Pang,[a] Jiaxing Jiang[a] and Shengzhong (Frank) Liu*[a,b]

Received 31st January 2016,
Accepted 12th March 2016

DOI: 10.1039/c6nr00880a

www.rsc.org/nanoscale

By taking advantages of both grinding and sonication, an effective exfoliation process is developed to prepare two-dimensional (2D) molybdenum oxide (MoO_3) nanosheets. The approach avoids high-boiling-point solvents that would leave a residue and cause aggregation. Gas sensors fabricated using the 2D-MoO_3 nanosheets provide a significantly enhanced chemical sensor performance. Compared with the sensors using bulk MoO_3, the response of the 2D-MoO_3 sensor increases from 7 to 33; the sensor response time is reduced from 27 to 21 seconds, and the recovery time is shortened from 26 to 10 seconds. We attribute the superior performance to the 2D-structure with a much increased surface area and reactive sites.

Introduction

As graphene, a two-dimensional (2D) carbon nanosheet, has displayed many extreme properties, including mechanical strength, electronic conductivity, stiffness, optical transparency, thermal conductivity, lightweight, and thinness,[1,2] that are craved for in many applications including electronics, photovoltaics, energy materials and medicine, a search for other 2D graphene-like materials is ever increasing. It is anticipated that the research effort will reach the similar intensity as that on graphene itself.[2,3]

There are only a few limited inorganic graphene analogues, among them, 2D oxides, *e.g.* layer-structured oxides including TiO_2, MoO_3, WO_3, mica, and a few perovskite-like crystals, are among the most studied for their stability at elevated temperature in air.[4–6] As they tend to partially lose oxygen at high temperature to become oxygen-deficient and they are strong adsorbents to organic molecules, they are the best candidates in chemical sensors for volatile organic compounds (VOC).[7,8] MoO_3, a wide bandgap semiconductor with its 2D layered structure and good sensor response to a variety of VOCs, is a model oxide in this category.

There have been a few techniques developed to prepare few-layered MoO_3 including mechanical exfoliation,[9] pulsed laser deposition,[10] thermal evaporation,[11] sputtering,[12] sol–gel,[13] spray pyrolysis,[14] chemical vapor deposition,[15] hydrothermal synthesis[16] and electro-deposition.[17] In particular, liquid-phase exfoliation has been adopted to produce single- and few-layered materials by simple grinding assisted sonication exfoliation in solvents[18,19] or aqueous surfactant solutions.[20,21] Here, sonication results in the exfoliation of the layered crystal into few-layered nanosheets in the presence of a stabilization agent like a surfactant and/or ligand to form complexes. Grinding assisted sonication exfoliation hence becomes one of the most attractive methods due to its high yield while avoiding the use of hazardous reagents. For example, Coleman has a detailed report[9] on the high yield exfoliation of 2D nanosheets to achieve concentrations as high as 0.3 mg ml^{-1} for MoS_2, 0.15 mg ml^{-1} for WS_2, and 0.06 mg ml^{-1} for BN. In the present work, the maximum concentration attained for MoO_3 (50% ethanol/water) is 0.182 mg ml^{-1}, comparable with the "high yield" generation of other 2D nanosheets.[9] The same group also studied the effect of sonication on 2D nanosheet fabrication and reported that the longer the sonication, the higher the concentration.[22]

In present work, a combination of grinding and sonication was used to cause exfoliation of the bulk α-MoO_3 crystals into single and few-layer nanosheets. In the meantime, a surfactant was used to stabilize them. A few solvents have been tested. It is interesting to see that a combination of two relatively poor solvents results in the best synergistic outcome. Moreover, it is found that the 2D-MoO_3 nanosheets are far more effective than bulk MoO_3 powder for chemical sensor application. Compared with the sensor using bulk MoO_3, the response of the present sensor using the 2D-MoO_3 nanosheets increases from 7 to 33. Besides, the sensor using the 2D-MoO_3 nanosheets has significantly a shorter response time as well as recovery time.

[a]*Key Laboratory of Applied Surface and Colloid Chemistry, National Ministry of Education; Shaanxi Engineering Lab for Advanced Energy Technology; School of Materials Science and Engineering, Shaanxi Normal University, Xi'an 710119, China. E-mail: szliu@dicp.ac.cn; Tel: +86-29-8153-0785*
[b]*Dalian Institute of Chemical Physics, iChEM, Dalian National Laboratory for Clean Energy, Chinese Academy of Sciences, Dalian, 116023, China*
†Electronic supplementary information (ESI) available. See DOI: 10.1039/c6nr00880a

Experimental

Fabrication of 2D MoO_3 nanosheets

1000 mg of the MoO_3 powder (99.95% purity, from Aladdin) was ground with 0.2 mL acetonitrile for 1 h. The powder was dispersed in a solvent. The solvent tested includes deionized water, 25 vol% ethanol/water solution, 50 vol% ethanol/water solution, 75 vol% ethanol/water solution, ethanol, iso-propyl alcohol (IPA), *N*,*N*-dimethylformamide (DMF), dimethyl sulfoxide (DMSO) respectively, then sonicated for 120 min, and centrifuged at 8000 rpm for 30 min at room temperature. The supernatant liquid containing 2D MoO_3 was collected. MoO_3 samples were then prepared for the characterization of their microstructure and properties. Fig. 1(a) shows a schematic illustration of the process.

Fabrication and test of gas sensors

The sensor structure is illustrated in Fig. 1(b). In brief, it was made of a ceramic thin film substrate printed with three pairs of Ag–Pd interdigitated electrodes. The supernatant liquid was dropcast onto the electrode surface, followed by drying on a hot plate at 70 °C. The gas-sensing properties of the samples were determined in a static flow system (CGS-4TPs, Beijing Elite Tech Co., Ltd, China). Test VOC was injected into the test chamber (1.8 L in volume) using a microliter syringe through the sample inlet. After the test VOC material was injected onto the hot evaporation stage, the target vapor was formed. When the sensor response reached a constant value, the test chamber was opened and the system exposed to an ambient atmosphere to measure its recovery in air. The resistance values of the gas sensors were measured at different operating temperatures adjusted by heating the sensor unit through a Thermo controller. The test was performed in a temperature range of 175–350 °C. The sensitivity, S, was determined as the ratio R_a/R_g, where R_a is the resistance in an ambient air atmosphere and R_g is the resistance in a tested gas atmosphere. The response time and recovery time are defined by the time spent for the sensor to achieve 90% of the total resistance change in the case of adsorption and desorption, respectively. Fig. 1(c) provides the equivalent circuit model for sensor testing. The heating voltage (V_h) was used to heat the sensor and control the operating temperature. The load resistance and the sensor are connected in series. When a voltage (V_c) was applied in the circuit, the output voltage (V_{out}) across the load resistance is measured as a function of gas used, $R_s = (V_c - V_{out})/V_{out} \times R_N$.

Structural characterization

The samples were characterized using UV-Vis-NIR spectroscopy (Lambda-950 spectrometer, Perkin Elmer, USA), X-ray diffraction (XRD, DX-2700 diffractometer employing a Cu-Kα source), Raman spectroscopy (Renishaw inVia micro-Raman spectrometer), transmission electron microscope (TEM, JEM-2100), atomic force microscopy (AFM, Multimode 8, Bruker).

Results and discussion

2D MoO_3 nanostructure characterization

All samples used for nanostructure characterization are from the suspension prepared using the 50 vol% ethanol/water solution. Fig. 2 shows the UV-Vis-NIR spectra of the MoO_3 nanosheet suspension and the bulk MoO_3. The distinct peaks at 220 and 256 nm are assigned to the excitonic absorption of the MoO_3 nanosheets.[23,24] It is known that the optical absorp-

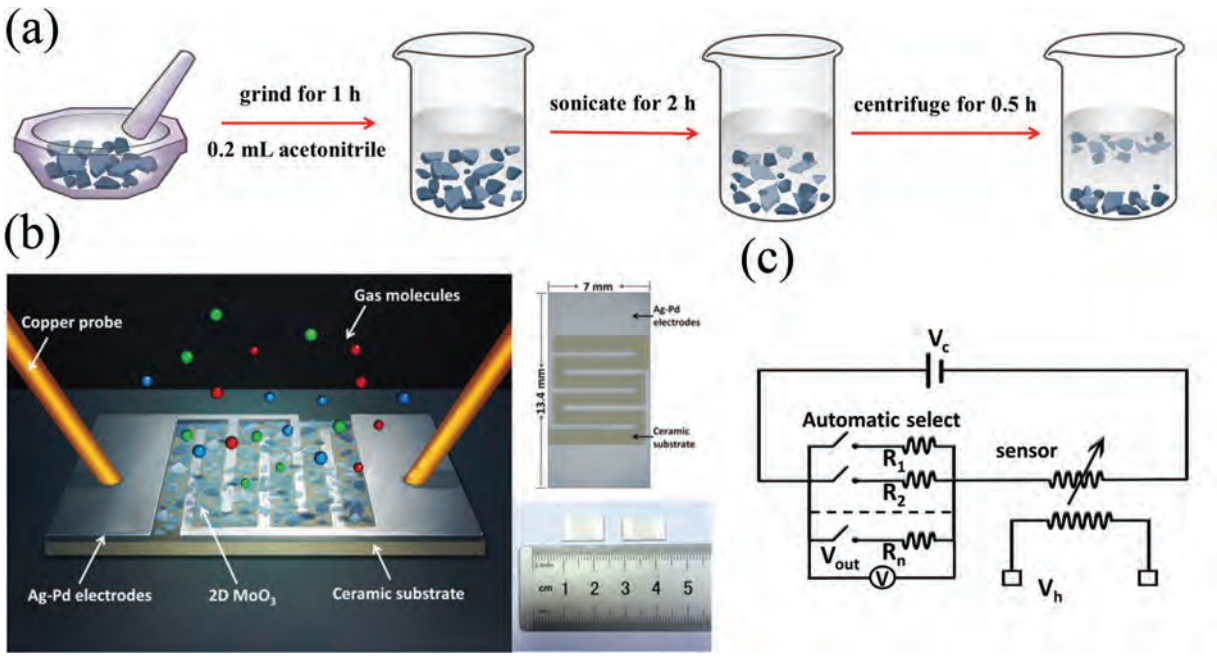

Fig. 1 (a) Three-step liquid exfoliation process. (b) Schematic illustration of the fabricated sensor. (c) Image of the operating principle.

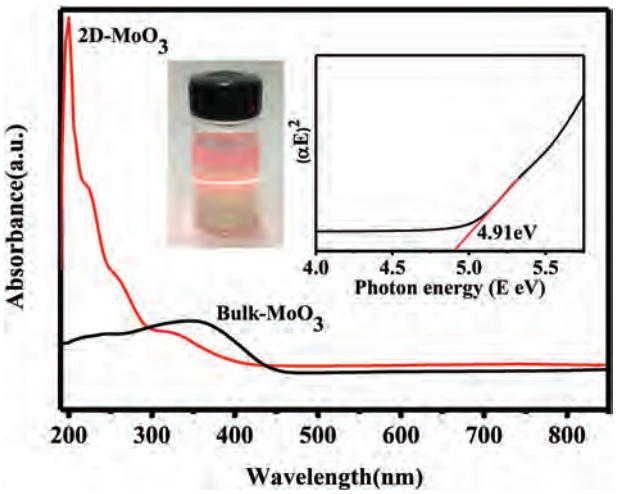

Fig. 2 UV-vis range absorbance spectra of the bulk MoO_3 crystal and exfoliated MoO_3 suspension.

tion of 2D MoO_3 exhibits a strong blue-shift when the lateral dimension reduces, as ascribed to the quantum size effect. As a consequence, the strong quantum confinement effect leads to the enhanced band gap opening. By plotting the square of the absorption energy (αE, where α is the absorbance and E is the photon energy) against E (right inset in Fig. 2), the direct band-gap energy is determined to be 4.91 eV, much larger than that from the bulk MoO_3 (~3.3 eV).

Fig. 3(a) shows the XRD patterns of the MoO_3 nanosheets in comparison with the bulk MoO_3 powder. Most of the peaks for these samples are indexed to orthorhombic MoO_3 (JCPDS 05-0508). The dominant peaks observed at 12.8, 25.7, and 39.1 corresponded to (020), (040), and (060) planes, respectively. This reveals that MoO_3 layers grow with strong preferential orientations of (100) and (001), consistent with our HRTEM analysis in Fig. 6(c).[23–26] The strong intensities of the reflection peaks of (0k0) with k = 2, 4, and 6 prove the existence of the lamellar structure.[11,25] In comparison, after exfoliation, the intensity of these peaks decrease significantly, clearly demonstrating that the layered MoO_3 has been successfully exfoliated as expected.

Raman spectroscopy was performed using a 532.2 nm excitation. Fig. 3(b) shows a comparison of Raman of bulk MoO_3 and 2D MoO_3 nanosheets in the range of 100–1100 cm^{-1}. The sharp peaks indicate that the corresponding vibrational modes are mostly due to a highly ordered structure. The strong, typical peaks at 154, 284, 671, 821 and 999 cm^{-1} were observed. The 154 cm^{-1} (A_g, B_{1g}) band originates from the translation of the rigid chains; the 284 cm^{-1} (B_{2g}, B_{3g}) band is a doublet composed of wagging modes of the terminal oxygen atoms (Mo=O vibration); the 336 cm^{-1} (B_{1g}, A_g) band is assigned to the Mo_3–O bending mode; and the 378 cm^{-1} (A_g) band is assigned to the Mo=O bending mode. The 671 cm^{-1} band (B_{2g}, B_{3g}) is an asymmetric stretching mode of the triply connected bridge–oxygen Mo_3–O bridge along the c-axis, which results from the edge-shared oxygen (Mo_3–O) in common with three adjacent octahedra. The intense Raman band at 821 cm^{-1} (A_g, B_{1g}) is a symmetric stretching mode of the terminal oxygen atoms or the doubly connected bridge–oxygen Mo–O–Mo, which results from corner-shared oxygen in common with two octahedra. The 991 cm^{-1} (A_g, B_{1g}) band is the asymmetric stretch of the terminal oxygen atom (Mo^{6+}=O) mode along the a and b axes, which results from an unshared oxygen, and it is responsible for the layered structure of α-MoO_3. All Raman peaks are in agreement with the results obtained from pure α-MoO_3.[25,27,28] The 336, 378, and 365 cm^{-1} peaks are assigned to O–Mo–O bending and scissoring modes, which become constantly weaker as the layered sheet becomes thinner.[27] The strong peaks include the 671 cm^{-1} peak which represents the triply coordinated oxygen stretching and the 821 cm^{-1} peak which is for the doubly coordinated oxygen (Mo_2–O) stretching mode. They assert the existence of the double-layer in the thinnest sheets formed on the surface.[25]

It is critical to ascertain the nature of the dispersed MoO_3. TEM analyses were conducted in order to investigate the dimensions and morphologies of the MoO_3 flake nanostructures from the suspension. The TEM image in Fig. 4(a) shows that the MoO_3 nanostructure mainly consists of

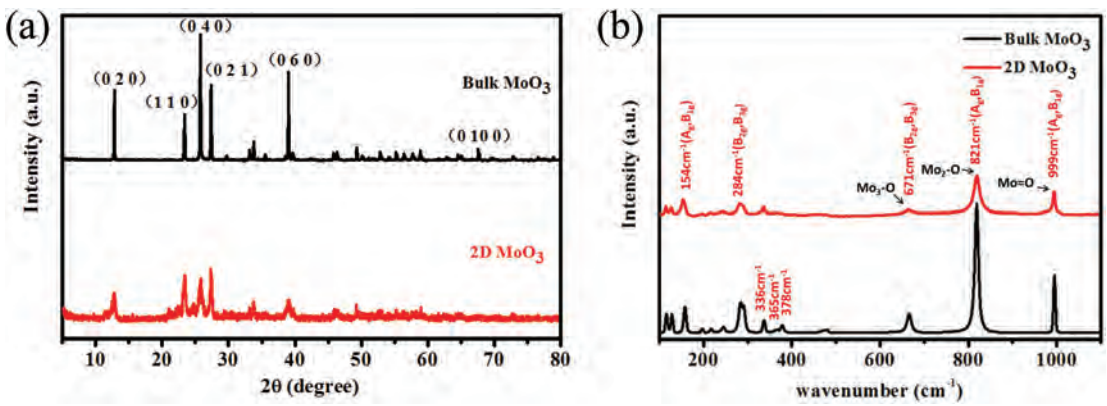

Fig. 3 (a) XRD pattern of bulk MoO_3 crystal and MoO_3 nanosheets dropped on glass. (b) Raman spectra of bulk MoO_3 crystal and MoO_3 nanosheets dropped on glass.

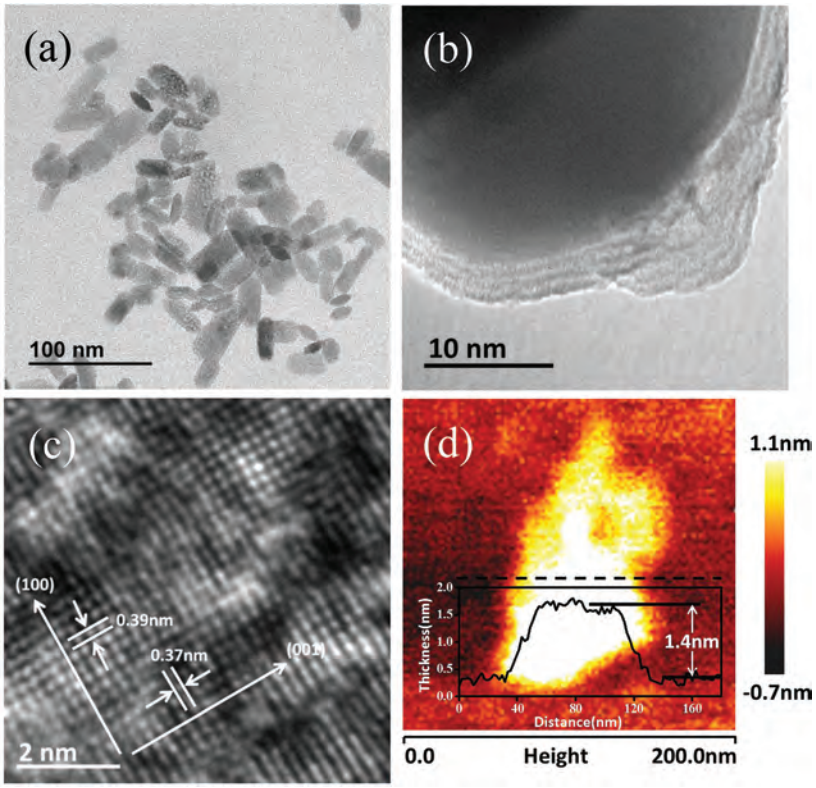

Fig. 4 (a) Representative TEM image of MoO_3 nanosheets. (b) Representative HRTEM image showing the layered nature of the MoO_3 nanosheets. (c) The corresponding distance between lattice fringes. (d) Representative AFM image of the MoO_3 nanosheet.

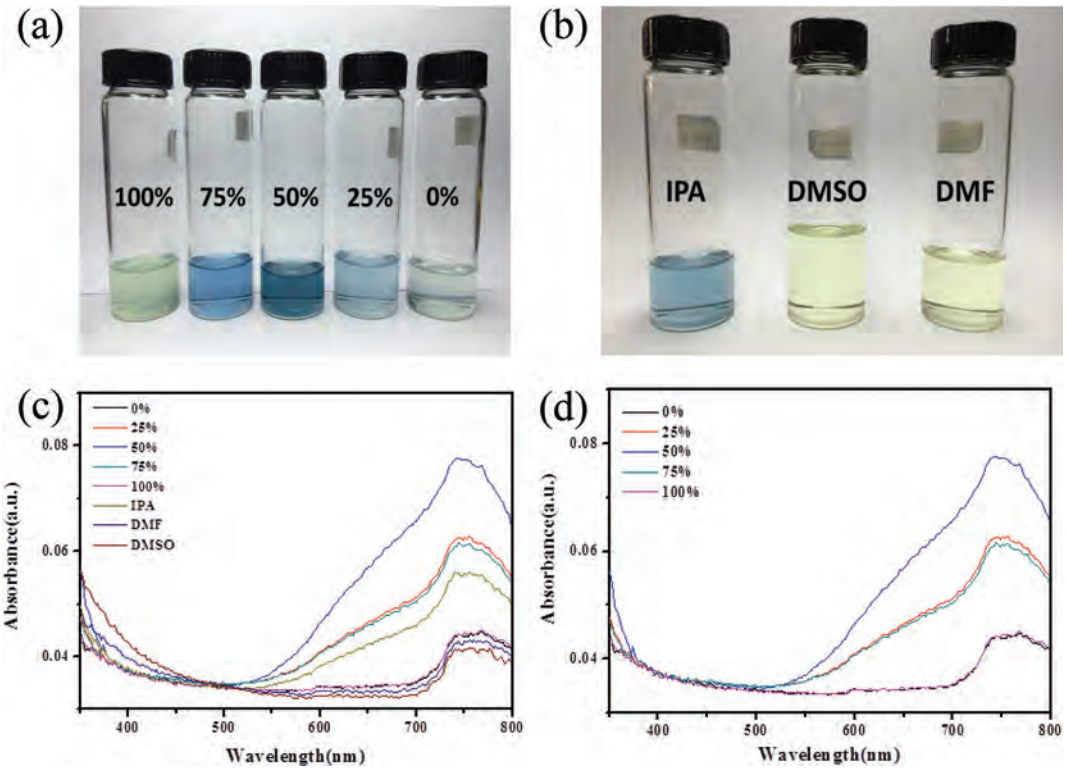

Fig. 5 (a) A photograph of the suspensions containing MoO_3 nanosheets prepared in different volume fraction of ethanol in water. (b) A photograph of suspensions containing MoO_3 nanosheets prepared in IPA, DMSO and DMF. (c) The optical absorbance of the MoO_3 nanosheet suspension using different solvents. (d) The optical absorbance of the MoO_3 nanosheet suspension using different volume fractions of ethanol in water.

nanosheets with various lateral dimensions in the range of 10–100 nm. Moreover, the HRTEM image was also acquired to assess the 2D nature and lattice arrangement of MoO_3 nanosheets. Fig. 4(b) shows that multi-layer edges can be observed near the periphery of these nanosheets. Fig. 4(c) clearly demonstrates the typical lattice spacing of highly ordered MoO_3 crystals as previously reported.[23–25] Two sets of parallel fringes in the image further reveal the well-defined crystalline lattices of MoO_3 nanosheets with spacings of 0.39 nm and 0.37 nm, corresponding to the *d*-spacing of the (100) and (001) planes of the orthorhombic phase of MoO_3, respectively.

To further confirm the morphology and thickness of the as-prepared MoO_3, AFM topography images of these nanostructures were analyzed. An AFM image of the surface morphology of an MoO_3 nanosheet placed onto a mica substrate is shown in Fig. 4(d). It is found that most particulates are 1.4 nm thick, corresponding to two-layered stacked MoO_3 sheets.[29,30]

MoO_3 nanosheets using different dispersion solvents

Liquid exfoliation has been successfully used to obtain highly dispersed suspensions of 2D-MoO_3 nanosheets. In the first place, we demonstrated a versatile mixed-solvent strategy for liquid exfoliation of MoO_3. By using an appropriate solvent, highly stable MoO_3 suspensions can be obtained in a low-boiling solvent. Herein, we tested a combination of two relatively poor solvents, ethanol and water, to make up a more powerful mixed-solvent.[21,31,32] We have obtained different concentrations of MoO_3 nanosheet suspensions by changing the ratio of ethanol to water as a liquid exfoliation solvent. Meanwhile, we also tested a few solvents with high solubility, such as IPA, DMSO, DMF.

The dispersion of nanomaterials in liquids can be partially predicted by the theory of Hansen solubility parameters (HSP),[9,22,33] a semi-empirical correlation developed to explain dissolution behavior.[33] Three HSP parameters are used to describe the character of a solvent or material: δ_D, δ_P, and δ_H, which are the dispersive, polar, and hydrogen-bonding solubility parameters, respectively. These parameters determine the concentration of MoO_3 that dispersed in solvents.

Fig. 5(a) shows a photograph of the suspension containing MoO_3 nanosheets using different volume fractions of ethanol in water. It is clear that MoO_3 nanosheets exhibit significantly

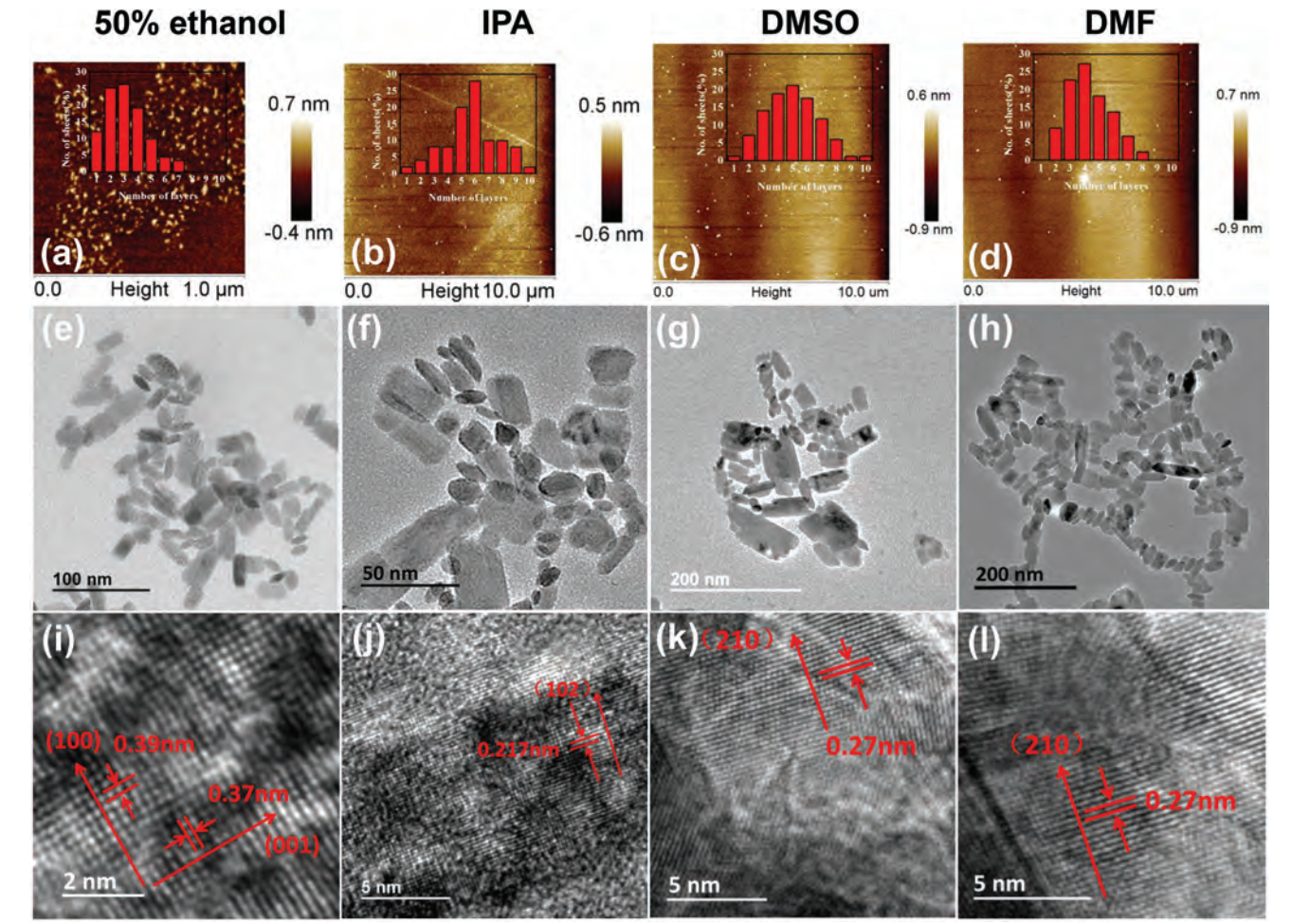

Fig. 6 (a–d) Statistical distribution of MoO_3 nanosheets thickness analysed from AFM images. (e–h) The lateral dimensions of MoO_3 nanosheets synthesized with different solvents analysed from TEM images. (i–l) The typical lattice spacing of highly ordered MoO_3 from TEM images.

different dispersion properties in ethanol/water mixtures with different ratios. It clearly shows that the MoO_3 nanosheet concentration in the dispersion is strongly dependent upon the ethanol/water ratio. Fig. 5(b) shows a photograph of suspensions prepared in IPA, DMSO and DMF. It means that different solvents have different abilities to disperse MoO_3 nanosheets. Fig. 5(c) and (d) present the optical absorbance of the MoO_3 nanosheets measured using UV-Vis-NIR spectroscopy, each sample showing a broad absorption band from ~550 nm to the NIR region, consistent with its blue color appearance.

To determine the concentration of the MoO_3 nanosheets in the supernatant from centrifugation, we measured the mass of MoO_3 nanosheets in the supernatant. In brief, take 10 mL of the supernatant, transfer it into a round-bottom flask, remove the solvent by evaporation, weigh the dried product to calculate the nanosheet concentration. Table S1† summarizes the concentration of the MoO_3 nanosheets attained in different solvents. It shows that the 50 vol% ethanol/water solution is more effective to disperse the MoO_3 nanosheets than other solvents, with the highest concentration 0.182 mg ml^{-1} harvested.

The thickness distribution and lateral dimensions of the MoO_3 nanosheet samples are analyzed using high resolution TEM and AFM images as shown in Fig. 6. The effect of the solvent selection upon the physical characteristics of the produced flakes becomes fairly evident. When DMF is used, it produces many thin flakes with a thickness ≤4 layers while IPA produces flakes with a tendency towards thicker >4 layers. The thinness of the flakes produced using DMSO shows a normal distribution from 2 to 8 layers, with the highest population at 5 layers. It appears that the 50 vol% ethanol/water solution produces nanosheets mostly with thickness ≤4 layers, suggesting that the solvent is effective not only in dispersing but also in exfoliating the MoO_3 nanosheets.

Gas sensing results

Before each sensor test, the device is always aged thermally at 200 °C, until the response curve is stable. This step removes volatile solvents. For the sensor test, the sensor was heated to the set temperature before R_a was measured for ~60 s in fresh air. The test VOC was then introduced into the sensor test chamber to measure R_g for ~200 s until R_g was stable. The

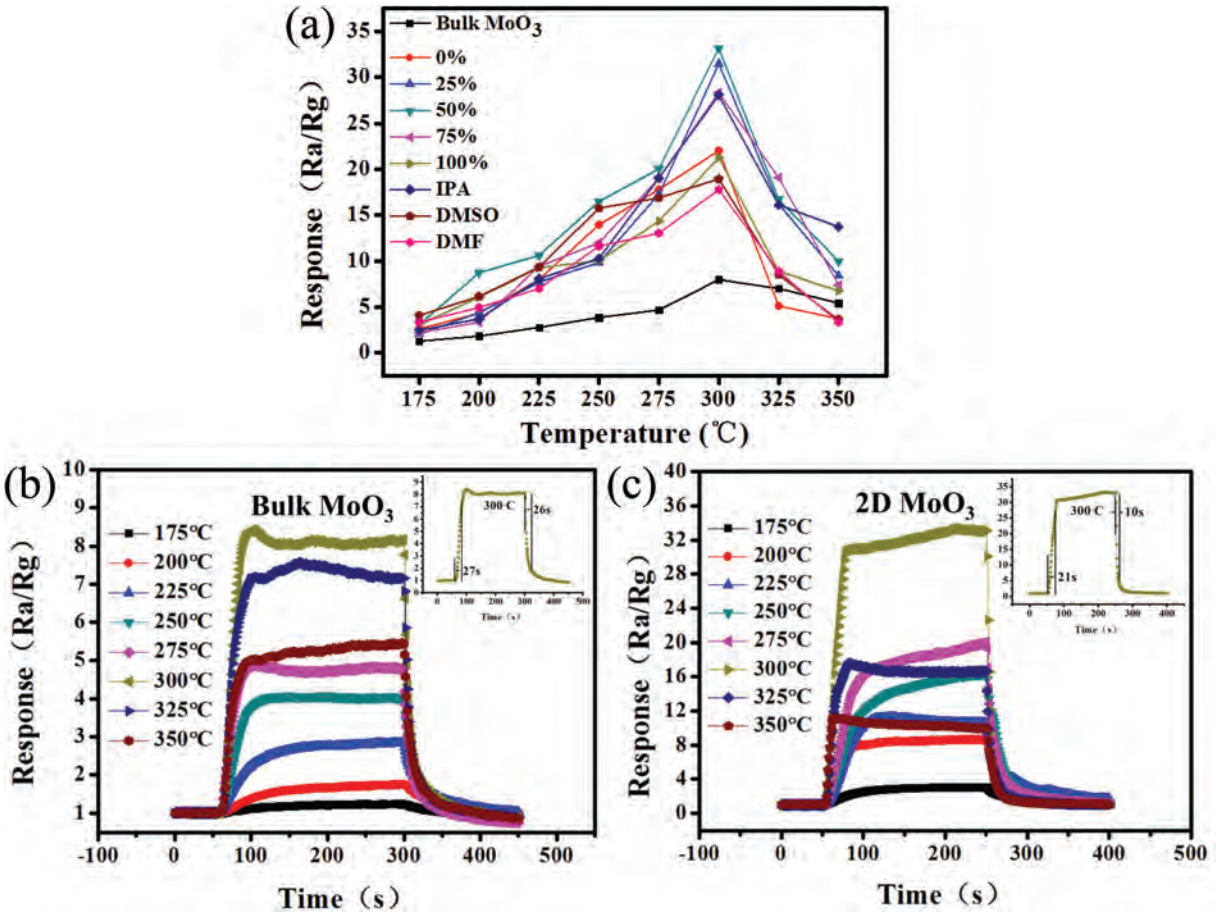

Fig. 7 (a) The results of the sensor response using bulk MoO_3 and MoO_3 nanosheets toward 100 ppm alcohol vapor at different operating temperatures. Transient sensor response toward 100 ppm alcohol vapor at different temperatures. The upper-right inset in each figure shows corresponding response and recovery curves for the senor at its optimum working temperature. (b) Bulk MoO_3; (c) MoO_3 nanosheets prepared in 50 vol% ethanol/water solution.

chamber was then opened to expose the sensor to fresh air to measure the resistance until it recovered to the initial value measured in fresh air.

At different working temperatures, the sensors were measured using a series of alcohol vapor concentrations. Fig. 7(a) shows the results of the sensor response using bulk MoO_3 and MoO_3 nanosheets. The MoO_3 nanosheets were obtained from different sonication solvents including deionized water, 25 vol% ethanol/water solution, 50 vol% ethanol/water solution, 75 vol% ethanol/water solution, ethanol, IPA, DMF and DMSO towards 100 ppm alcohol vapor. The optimum working temperature for MoO_3 is 300 °C for all samples. It is well known that gas sensing involves a few major steps: adsorption/desorption of the target gas on the sensor material, and the reaction of the adsorbed species on the material. In the lower temperature range, as the reaction rate is increased with the operating temperature, so does the sensor response. When the operating temperature surpasses a certain optimal temperature, in the present case (T = 300 °C), the desorption process outweighs other factors and therefore the sensor response drops as the operation temperature further goes up. At the optimum working temperature, the sensor response value of bulk MoO_3 is 8, and the sensor response values of MoO_3 nanosheets are 22, 31, 33, 28, 21, 28, 19 and 18 respectively, all are significantly higher than that of the bulk MoO_3. The sensor performance is shown in Fig. S1 and Table S2.† The MoO_3 nanosheets dispersed in the 50 vol% ethanol/water solution show the response up to 33, ~3 times higher than the value of the bulk MoO_3. It should be noted that the performance of the sensors made of MoO_3 nanosheets obtained from DMSO and DMF are lower than others. As both DMSO and DMF solvents have high boiling points, it is difficult to remove them during the MoO_3 nanosheet device fabrication. It has been reported by Hernandez that the remaining solvents can cause aggregation during the slow solvent evaporation,[31,34] leading to a lower sensor response. Furthermore, Fig. 7(b) and (c) and Table S3† show the sensor response time. It is found that both the sensor response and recovery time are reduced significantly. More specifically, the response time is reduced to 21 seconds from 27 seconds for the reference; meanwhile, the recovery time sharpened from 26 to 10 seconds. It appears to be apparent that the MoO_3 nanosheet sample exhibits significantly enhanced alcohol vapor sensing performance compared to the bulk MoO_3.

Fig. 8(a) shows the response of the best sensor made of MoO_3 nanosheets toward different alcohol vapor concentrations ranging from 10 to 500 ppm at the optimum working temperature. It shows that all responses increase with alcohol vapor concentration, at 10 ppm, the sensor response is only 11; when the concentration was increased to 100 ppm, the response increased to 33; on further increasing the concentration to 500 ppm, the response increased to 140.

The gas sensors for practical applications are required to have not only a good response, but also to have good selectivity to the test gas. We therefore studied the sensor responses to other VOCs (C_4H_8O, C_6H_6, CH_3CHO, CH_3COCH_3, CH_3OH, $CHCl_3$, HCOOH) at 300 °C. The measured results using 100 ppm VOCs are shown in Fig. 8(b). It is clear that sensors have a relatively high response to alcohol vapor, but negligible responses to other VOCs. The sensor response value to alcohol vapor is 3–7 times higher than to others. It is concluded that MoO_3 has good selectivity to the alcohol vapor. The enhanced sensor performance is attributed to a much increased surface area and reactive sites.[30]

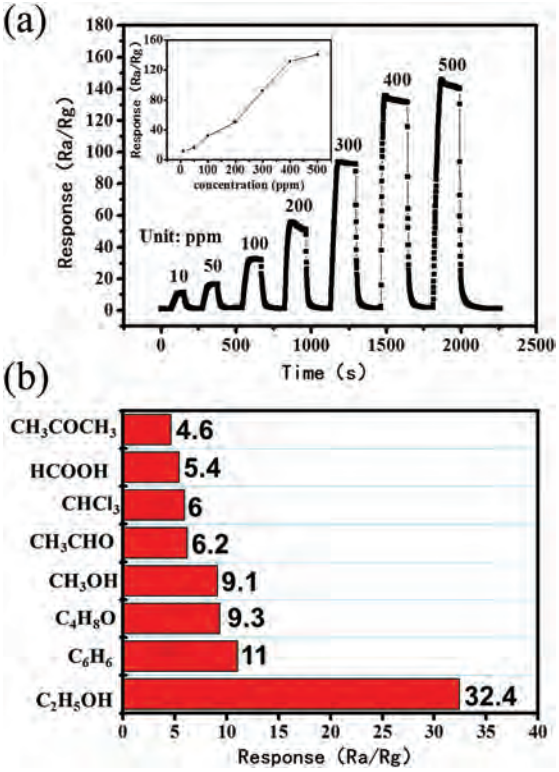

Fig. 8 (a) Transient response and recovery curves of the best sensor made of MoO_3 nanosheets toward different alcohol vapor concentration ranging from 10 to 500 ppm at the optimum working temperature. (b) Sensor responses of sensors made of MoO_3 nanosheets toward 100 ppm VOCs.

Conclusion

In conclusion, a 2D-MoO_3 nanosheet suspension was prepared using an effective exfoliation technique that takes advantages of both grinding and sonication. As demonstrated above, a combination of two relatively poor solvents, ethanol and water in a 50 : 50 ratio, works best for exfoliating MoO_3. Compared with the sensors using the bulk MoO_3, the 2D-MoO_3 nanosheet sensor shows significantly higher response, faster response and recovery time. We attribute this superior performance to the layered structure with a much increased surface area and reactive sites. It appears that the 2D-MoO_3 nanosheets prepared using the present technique are advantageous for sensors and related applications.

Acknowledgements

The authors acknowledge support from the National University Research Fund (GK261001009), the Changjiang Scholar and Innovative Research Team (IRT_14R33), the Overseas Talent Recruitment Project (B14041) and the Chinese National 1000-talent-plan program.

References

1 F. Bonaccorso, Z. Sun, T. Hasan and A. C. Ferrari, *Nat. Photonics*, 2010, **4**, 611–622.
2 A. K. Geim and I. V. Grigorieva, *Nature*, 2013, **499**, 419–425.
3 B. Radisavljevic, A. Radenovic, J. Brivio, V. Giacometti and A. Kis, *Nat. Nanotechnol.*, 2011, **6**, 147–150.
4 S. Z. Butler, S. M. Hollen, L. Cao, Y. Cui, J. A. Gupta, H. R. Gutierrez, T. F. Heinz, S. S. Hong, J. Huang, A. F. Ismach, E. Johnston-Halperin, M. Kuno, V. V. Plashnitsa, R. D. Robinson, R. S. Ruoff, S. Salahuddin, J. Shan, L. Shi, O. M. G. Spencer, M. Terrones, W. Windl and J. E. Goldberger, *ACS Nano*, 2013, **7**, 2898–2926.
5 M. Xu, T. Liang, M. Shi and H. Chen, *Chem. Rev.*, 2013, **113**, 3766–3798.
6 M. Li, Q. Ma, W. Zi, X. Liu, X. Zhu and S. F. Liu, *Sci. Adv.*, 2015, **1**, 1–7.
7 K. S. Novoselov, D. Jiang, F. Schedin, T. J. Booth, V. V. Khotkevich, S. V. Morozov and A. K. Geim, *Proc. Natl. Acad. Sci. U. S. A.*, 2005, **102**, 10451–10453.
8 M. Osada and T. Sasaki, *Adv. Mater.*, 2012, **24**, 210–228.
9 J. N. Coleman, M. Lotya, A. O'Neill, S. D. Bergin, P. J. King, U. Khan, K. Young, A. Gaucher, S. De, R. J. Smith, I. V. Shvets, S. K. Arora, G. Stanton, H. Y. Kim, K. Lee, G. T. Kim, G. S. Duesberg, T. Hallam, J. J. Boland, J. J. Wang, J. F. Donegan, J. C. Grunlan, G. Moriarty, A. Shmeliov, R. J. Nicholls, J. M. Perkins, E. M. Grieveson, K. Theuwissen, D. W. McComb, P. D. Nellist and V. Nicolosi, *Science*, 2011, **331**, 568–571.
10 S. S. Sunu, E. Prabhu, V. Jayaraman, K. I. Gnanasekar and T. Gnanasekaran, *Sens. Actuators, B*, 2003, **94**, 189–196.
11 M. B. Rahmani, S. H. Keshmiri, J. Yu, A. Z. Sadek, L. Al-Mashat, A. Moafi, K. Latham, Y. X. Li, W. Wlodarski and K. Kalantar-zadeh, *Sens. Actuators, B*, 2010, **145**, 13–19.
12 A. K. Prasad, P. I. Gouma, D. J. Kubinski, J. H. Visser, R. E. Soltis and P. J. Schmitz, *Thin Solid Films*, 2003, **436**, 46–51.
13 K. Galatsis, Y. X. Li, W. Wlodarski and K. Kalantar-zadeh, *Sens. Actuators, B*, 2001, **77**, 478–483.
14 H. M. Martínez, J. Torres, M. E. Rodríguez-García and L. D. López Carreño, *Physica B*, 2012, **407**, 3199–3202.
15 S. Ashraf, C. S. Blackman, G. Hyett and I. P. Parkin, *J. Mater. Chem.*, 2006, **16**, 3575–3582.
16 T. Brezesinski, J. Wang, S. H. Tolbert and B. Dunn, *Nat. Mater.*, 2010, **9**, 146–151.
17 D. D. Yao, J. Z. Ou, K. Latham, S. Zhuiykov, A. P. O'Mullane and K. Kalantar-zadeh, *Cryst. Growth Des.*, 2012, **12**, 1865–1870.
18 G. Cunningham, M. Lotya, C. S. Cucinotta, S. Sanvito, S. D. Bergin, R. Menzel, M. S. P. Shaffer and J. N. Coleman, *ACS Nano*, 2012, **6**, 3468–3480.
19 A. O'Neill, U. Khan and J. N. Coleman, *Chem. Mater.*, 2012, **24**, 2414–2421.
20 M. Lotya, Y. Hernandez, P. J. King, R. J. Smith, V. Nicolosi, L. S. Karlsson, F. M. Blighe, S. De, Z. Wang, I. T. McGovern, G. S. Duesberg and J. N. Coleman, *J. Am. Chem. Soc.*, 2009, **131**, 3611–3620.
21 Y. Yao, L. Tolentino, Z. Yang, X. Song, W. Zhang, Y. Chen and C.-p. Wong, *Adv. Funct. Mater.*, 2013, **23**, 3577–3583.
22 J. N. Coleman, *Adv. Funct. Mater.*, 2009, **19**, 3680–3695.
23 S. Balendhran, S. Walia, H. Nili, J. Z. Ou, S. Zhuiykov, R. B. Kaner, S. Sriram, M. Bhaskaran and K. Kalantar-zadeh, *Adv. Funct. Mater.*, 2013, **23**, 3952–3970.
24 M. B. Sreedhara, H. S. Matte, A. Govindaraj and C. N. Rao, *Chem. – Asian. J.*, 2013, **8**, 2430–2435.
25 K. Kalantar-zadeh, J. Tang, M. Wang, K. L. Wang, A. Shailos, K. Galatsis, R. Kojima, V. Strong, A. Lech, W. Wlodarski and R. B. Kaner, *Nanoscale*, 2010, **2**, 429–433.
26 J. Z. Ou, J. L. Campbell, D. Yao, W. Wlodarski and K. Kalantar-zadeh, *J. Phys. Chem. C*, 2011, **115**, 10757–10763.
27 A. Chithambararaj and A. C. Bose, *Beilstein J. Nanotechnol.*, 2011, **2**, 585–592.
28 O. Lupan, V. Cretu, M. Deng, D. Gedamu, I. Paulowicz, S. Kaps, Y. K. Mishra, O. Polonskyi, C. Zamponi, L. Kienle, V. Trofim, I. Tiginyanu and R. Adelung, *J. Phys. Chem. C*, 2014, **118**, 15068–15078.
29 S. Balendhran, S. Walia, M. Alsaif, E. P. Nguyen, J. Z. Ou, S. Zhuiykov, S. Sriram, M. Bhaskaran and K. Kalantar-zadeh, *ACS Nano*, 2013, **7**, 9753–9760.
30 M. M. Y. A. Alsaif, S. Balendhran, M. R. Field, K. Latham, W. Wlodarski, J. Z. Ou and K. Kalantar-zadeh, *Sens. Actuators, B*, 2014, **192**, 196–204.
31 A. O'Neill, U. Khan, P. N. Nirmalraj, J. Boland and J. N. Coleman, *J. Phys. Chem. C*, 2011, **115**, 5422–5428.
32 K. G. Zhou, N. N. Mao, H. X. Wang, Y. Peng and H. L. Zhang, *Angew. Chem., Int. Ed.*, 2011, **50**, 10839–10842.
33 C. M. Hansen, *Hansen Solubility Parameters - A User's Handbook*, CRC Press, Boca Raton, FL, 2007.
34 Y. Hernandez, V. Nicolosi, M. Lotya, F. M. Blighe, Z. Sun, S. De, I. T. McGovern, B. Holland, M. Byrne, Y. K. Gun'Ko, J. J. Boland, P. Niraj, G. Duesberg, S. Krishnamurthy, R. Goodhue, J. Hutchison, V. Scardaci, A. C. Ferrari and J. N. Coleman, *Nat. Nanotechnol.*, 2008, **3**, 563–568.